

Detection of the Permanent Strain Offset Component of Gravitational-Wave Memory in Black Hole Mergers

JEFFREY D. SCARGLE¹

¹*Astrobiology and Space Science Division
Planetary Systems Branch
NASA Ames Research Center
Moffett Field, CA 94035, USA
Jeffrey.D.Scargle@nasa.gov
jeffscargle@gmail.com*

ABSTRACT

This letter reports the first direct measurements of the permanent space-time strain component of the gravitational-wave *memory* effect, predicted by general relativity to accompany black hole merger events. By ignoring the details of how the memory effect develops over time, this approach circumvents the need for precise modeling of the non-memory, linear memory, and nonlinear memory signals. Applied to a selection 64 observations of black hole merger events in the LIGO/Virgo Gravitational Wave Transient Catalog, this analysis yields a mixture of probable detections and upper limits. These results are supported by both individual and ensemble statistical significance analyses, based on analyzing the merger events – and a large number of time intervals shifted away from them – in exactly the same way.

Keywords: Gravitational Waves, Gravitational Memory, General Relativity

1. GRAVITATIONAL-WAVE MEMORY

According to general relativity, any gravitational wave is accompanied by permanent space-time changes, called *memory* effects. Space-time is an abstract concept, and its distortion in the form of compressive or expansive *strain* is not something that is perceptible in every day life or even in physics labs, other than in advanced laser interferometers dedicated to measuring it. Hence it is difficult to develop a clear intuitive feeling for space-time itself, space-time strain, and the meaning of a permanent change in it. Specific predictions of *gravitational-wave memory* arise in linear theory, and the gravitational waves themselves are an additional source of (non-linear) memory, which must accompany any gravitational wave signal. These effects, including “gravitons emitting gravitons,” the *Christodoulou effect*, yield the potential for new tests of general relativity in the non-linear regime.

1.1. Theory

The seminal work by Braginsky and Thorne (1987) and Thorne (1992) (with references to some precursor ideas) has spawned a still-active body of research, too large to detail here. Flanagan et al (2019, 2020) develop a general framework for persistent gravitational observables, of which memory is a special case. Linear and nonlinear (now often called *ordinary* and *null*) memory effects have been investigated by several authors (Favata 2010; Pollney and Reisswig 2011; Bian, Cai, Cao et al. 2020; Grant and Nichols 2020; Liu, He and Cao 2021; Khera, Krishnan, Ashtekar and De Lorenzo 2021; Mitman, Iozzo, Khera et al. 2021). Zhang et al (2017) and Divakarla and Whiting (2021) raise the possibility of non-zero asymptotic relative velocities of the test mirrors. This effect would presumably face even more difficult obstacles than the displacements studied here – simple *strain offsets*.

1.2. Detection Methods

Any detection scheme must mediate between two opposing issues. On the one hand, in contrast to an oscillation, a permanent strain offset is in essence a one time step, sometimes called a DC effect in electronics. Such a signal is

suppressed due to several realities: the presence of strong seismic and other noise at low frequencies, the suppression of low frequency noise in the public data and standard data analysis pipelines, and the tendency of the instrument to null out such offsets relatively quickly. On the other hand, the time scale of the development of memory strain is the same as that of the rise and fall of the envelope of the oscillations during the merger, thus yielding significant variability at moderately higher frequencies.

To be more quantitative, compare the amplitude spectrum of the simple analytic memory model discussed by Favata (2010) – with its rise from 0 to 1 described by the hyperbolic tangent function – to that for the numerical relativity curve for GW 150914 on the Gravitational Wave Open Science Center (GWOSC) web site at https://losc.ligo.org/s/events/GW150914/GW150914_4_NR_waveform.txt. This comparison shows both spectra to be roughly parallel $1/f$ curves over much of the region of interest but with the memory spectrum having considerably more amplitude below and above these limits. Normalized by the total at frequencies < 300 Hz, the integrated amplitude spectrum of GW 150914 below 10 Hz is 2% compared to 42% for the toy memory model; above 300 Hz the figures are 13% vs 64 %. All things considered, the important frequency ranges for merger and memory signals are similar, but with low frequencies somewhat more important for the latter. Early work (Braginsky and Thorne 1987; Thorne 1992; Kennefick 1994) exploring the severe limits on data analysis methods reached similar conclusions, expressed in a slightly different way: memory detection is optimal in the frequency range of LIGO’s maximum sensitivity.

1.3. Previous Detection Research

Previous detection attempts have uniformly failed to yield significant evidence for the presence of memory effects, and have not reported upper limits as such. These studies have utilized numerical relativity computations jointly modeling the unfolding of the merger itself and the buildup of memory effects (Kennefick 1994; Lasky et al. 2016; Yang and Martynov 2018; Johnson et al 2019; Boersma, Nichols and Schmidt 2020; Hübner, Lasky and Thrane 2020, 2021; Zhao, Liu, Cao and He 2021). Several reports of Bayesian posteriors and other information for specific merger events (Hübner, Lasky and Thrane 2020, 2021; Khera, Krishnan, Ashtekar and De Lorenzo 2021) seem to be essentially upper limits. For 48 events, including many of the same observations considered here, Zhao, Liu, Cao and He (2021) go further by assessing posteriors with Kullback-Leibler differences from assumed prior distributions, which however do not directly translate to statistical significances. They state “... we found 4 GW memory measurements definitely tell the signs of the memory on LIGO detectors.” For GW190412, GW190519 and GW190910 their posteriors appear to be consistent with the upper limits reported here (see Table 1). Their fourth event (GW190814) did not pass the selection criterion discussed here in §2.1 because the time-frequency distributions are diffusely scattered over more than 0.3 seconds with unclear start and stop times. The trials factor issue (see §5) was not addressed by these authors.

No doubt detailed joint modeling will ultimately be definitive. However it faces considerable difficulties through the need for detailed, accurate models of both the oscillatory and memory components, plus reliable determination of several model parameters – masses, spins, and orientations. Furthermore, this kind of mixture model problem tends to face uniqueness issues that can make it close to being ill-posed (Acton 1990). And finally, the relevant numerical relativity effort is not a settled activity, but comprises intensive on-going research using a variety of approximation schemes.

1.4. Measuring the Permanent Strain Offset

Detection of the full memory signal is clearly a very hard problem – in a sense even harder than detection of the merger itself, due to the added complexity in jointly modeling both components. Of course knowing precisely when the memory effect will occur (concurrent with the merger event itself) greatly facilitates its detection. In addition, the analysis described here alleviates the difficulties discussed in §1.3 by measuring only the magnitude of the permanent strain offset, ignoring the form of the development of the memory and merger components. A toy step function representation of the memory signal informs the definitions of the averaging intervals, as will be described in §3.1, but no actual modeling is required.

The approach proposed here simply compares the average strains before and after the event. Data *during* the events are largely ignored, serving only two purposes: to demarcate the intervals for averaging the pre- and post-event strains, and to normalize the permanent strain offset by the maximum strain during the event. Conveniently this relative change is the quantity discussed in most of the theoretical papers, and is self-calibrating. Statistical significance is assessed in much the same way as in event detection: apply the same estimation procedure on time-shifted data.

The next sections describe the two major data analysis elements: the quotidian but crucial step of cleaning the raw data of the noise that dwarfs any gravitational-wave signal – merger or memory – and the method for estimating the permanent strain offset (memory); the results are described in §4.

2. DATA PRE-PROCESSING

Strain time series, sampled at 16 kHz over intervals of 4096 seconds approximately centered on the merger events, were downloaded from the GWOSC site (Abbott et al. 2021) as constituted in July of 2021. These data series are called *observations* below. There can be one, two or three of them for each event, from the Hanford, Livingston and/or Virgo observatories. Events flagged as marginal and observations with missing data and were generally not included. GW 191223 and 191225, 62 and 63 in Table 1, included due to their remarkable time-frequency patterns, are deemed likely to be glitches. The following processing steps are listed in the order in which they are applied to the time series. In several cases a number of choices will be considered, and §4 describes an adaptive procedure for selecting the best from among them.

The term *event* throughout refers to the merger as embodied in the chirp signal, from inspiral to ring-down, but excluding the intervals selected for the pre-event and post-event strain averaging.

2.1. Data Selection

Memory estimation by subtracting pre-event from post-event strain requires scrupulous avoidance of the potentially confounding contribution from the event itself. Therefore those cases were selected where the beginning and end of the merger signal can be reliably estimated from the time-frequency distributions displayed at the GWOSC web site. In those few cases where the temporal confinement of the visible power is ambiguous due to low signal-to-noise in the leading and trailing parts of the time-profile, a conservative choice was made – overestimating the extent of the event. In total 64 observations (26 from Hanford, 35 from Livingston, and 3 from Virgo) from 40 different black hole mergers, were selected for analysis.

For the most part the stop time is cleanly defined, due to the rapidity of the ring-down portion of the signal. Errors in assigning start times are almost automatically mitigated: the approximately sinusoidal strain early in the in-spiral phase will largely average to zero. To enhance these insensitivities and mitigate any subjectivity in their visual estimation, the measured start and stop times were extended to include the previous and subsequent nodes of the oscillation, respectively – determined via zero crossings. Accordingly any unwanted contribution of merger strain due to a late start time or an early end time will closely sum to zero.

The steps described next comprise the standard pre-processing approach adapted to the present purpose of detecting non-oscillatory strain. Our goals include avoiding any further attenuation of low-frequency information (i.e. no high-pass filtering; cf. §2.5), and minimizing the number of tunable parameters – this largely to enable an objective analysis of the statistical significance of any detections. After ensuring zero-mean and convenient normalization of the full time series, the follow steps were applied.

2.2. Centering the Event

In the public data files the merger event time is close to, but not exactly at, the midpoint of a 4096 sec interval. It was discovered that this offset, typically a fraction of a second, makes a noticeable difference in the analysis results. With tapering (§2.3) symmetric about the midpoint, an offset signal would occur on a sloping part of the taper, yielding a potential bias that could masquerade as a memory effect. Hence the data sequences were shifted to bring the mid-point of the event – i.e. the midpoint between the start and stop times determined in the manner described above in §2.1 – to the center of the interval. The empty interval thus generated at the end of the full time series was filled with an auto-regressive extrapolation, to avoid any possible effect of the discontinuity that wrap-around produces.

2.3. Tapering

The importance of controlling Fourier phase modulations and spectral leakage has been emphasized in many publications and GWSOC tutorials. The widely adopted countermeasure is to carry out Fourier analysis on the time series multiplied by a window function, or *taper*, down-weighting the ends of the interval and smoothing the spectrum. From

among the dozens of tapers in common use,¹ most GW analyses have chosen the classic Tukey taper or more recent alternatives (McKechan, Robinson and Sathyaprakash 2010) with little or no justification beyond that discussed in footnote 1. It is often thought that there is no unique, or favored, windowing method. However Thomson (1982) rigorously derived tapers that explicitly minimize spectral leakage over all possible taper shapes. The resulting *multi-tapers* are a family of eigenfunctions (discrete prolate spheroidal wave functions, traditionally called Slepians) arising in the maximization of the power contained in the main lobe of the spectral response function (Slepian 1978; Thomson 1982; Percival and Walden 1993). In addition to reducing variance the higher order tapers apply greater weight at the beginning and end of the interval, thereby recovering information that is degraded by standard tapers. This feature is less important for the well-centered events analyzed here, but might be useful in other contexts, such as detection of unmodeled bursts that can occur anywhere in the interval.

Four tapers were evaluated: (1) Tukey, (2) the zero-order Slepian function, (3) the zero-order and first-order Slepians, averaged, and (4) the zero- first- and second-order Slepians, averaged. The averages were not of the tapers themselves, but of the tapered data after whitening. Taper symmetry is important for the reasons discussed in §2.2. Since the first order Slepian function is antisymmetric, it was applied both in direct and time-reversed form, symmetrizing the result. As described in §4 the choice of these tapers was determined using an optimization criterion separately for each observation; in only one-quarter of the cases did the Tukey taper outperform Thomson’s Slepian tapers.

2.4. Whitening

Because of the strong, correlated, and highly non-normal noise characteristic of GW strain data, whitening is also crucial and was effected with this formula:

$$h_{\text{white}}(t) = \text{IFFT}\left\{\frac{\text{FFT}[w(t)h(t)]}{S(\omega)}\right\}, \quad (1)$$

where $h(t)$ is the strain time series, $w(t)$ the *taper window*, and FFT and IFFT are the fast Fourier transform and its inverse. Three estimators for the power spectrum $S(\omega)$ were compared: the phase-only or unsmoothed Fourier power spectrum of $h(t)$, and the block-averaged Welch estimator (with the commonly used 4-second blocks) both with and without 2-second overlap. Each of the four tapers $w(t)$ in §2.3 were used – and for the Welch estimators applied both to the numerator of Eq. (1) and to the block data implicit in the denominator – yielding a total of 12 alternative whitening procedures.

2.5. Bandpass Filtering

The issue of the scale/frequency content of the memory signal is not as simple as thinking of it as a “DC” signal. In principle the scales of variability of the *permanent* strain offset are unlimited on the long end and extend to the shortest scales associated with the rapid memory buildup predicted to occur during the merger. Here this range extends from the full observation interval of 4096 seconds to a few milliseconds – frequencies from 10^{-4} to 10^3 Hz.

As adumbrated in §1.2 the rapid increase in noise below 10 Hz, the filtering of the public GWOSC data below 8 Hz, and declining instrumental response at low frequencies all need to be considered. Accordingly the pipeline adopted here avoids any further attenuation of variability of low frequencies, other than that implicitly provided by the equalization inherent in whitening process just described. The high frequency issue here is similar to that for the event itself – tradeoff of sensitivity to signal against sensitivity to noise. The analysis was carried out using a 64th-order finite impulse low-pass filter, with 9 values for the cutoff – from 100 to 500 Hz in steps of 50 Hz.

¹ These ad hoc tapers are merely guesses, largely without a clear principle or quantitative metric; later their properties are studied and compared one against another, and deemed “good.” In spite of the characterization of the huge amount of work quantifying leakage properties (and comparing one taper to another) as “window design,” the proposed tapers are not generated from an unambiguous quantitative principle, as are the Thomson tapers.

3. MEASURING THE STRAIN OFFSET

We are now ready to extract measurements of the strain offset, and relevant statistical quantities, from the strain time series cleaned as described in the previous section. After setting the intervals over which to average the strains, there are several ways that the averaging can be carried out.

3.1. Defining Pre-Event and Post-Event Averaging Intervals

As emphasized e.g. by Braginsky and Thorne (1987) lengths of averaging intervals are crucial parameters for detection of memory effects. Here a different approach is useful to quantify this issue. Figure 1 shows the response of a sample pre-processing procedure to the addition of the simple hyperbolic tangent memory expression² mentioned in §1.2. Of crucial importance is *the decay of the strain offset on a time scale of a few times the duration of the merger event*. Such decay to zero – called *reversion* hereafter – does not include effects of the interferometric detector system, which presumably yields even somewhat faster decay. (Note the small negative offset in the pre-event strain, and the preservation of short time-scale structure.)

In principle, in estimating the “permanent” strain offset predicted by theory, one would like to average over an infinite length of time. In reality it is necessary to take account of the reversion of the observable memory signal due to effects of the instrument and the data analysis. These considerations led to the *adoption of pre-event and post-event*

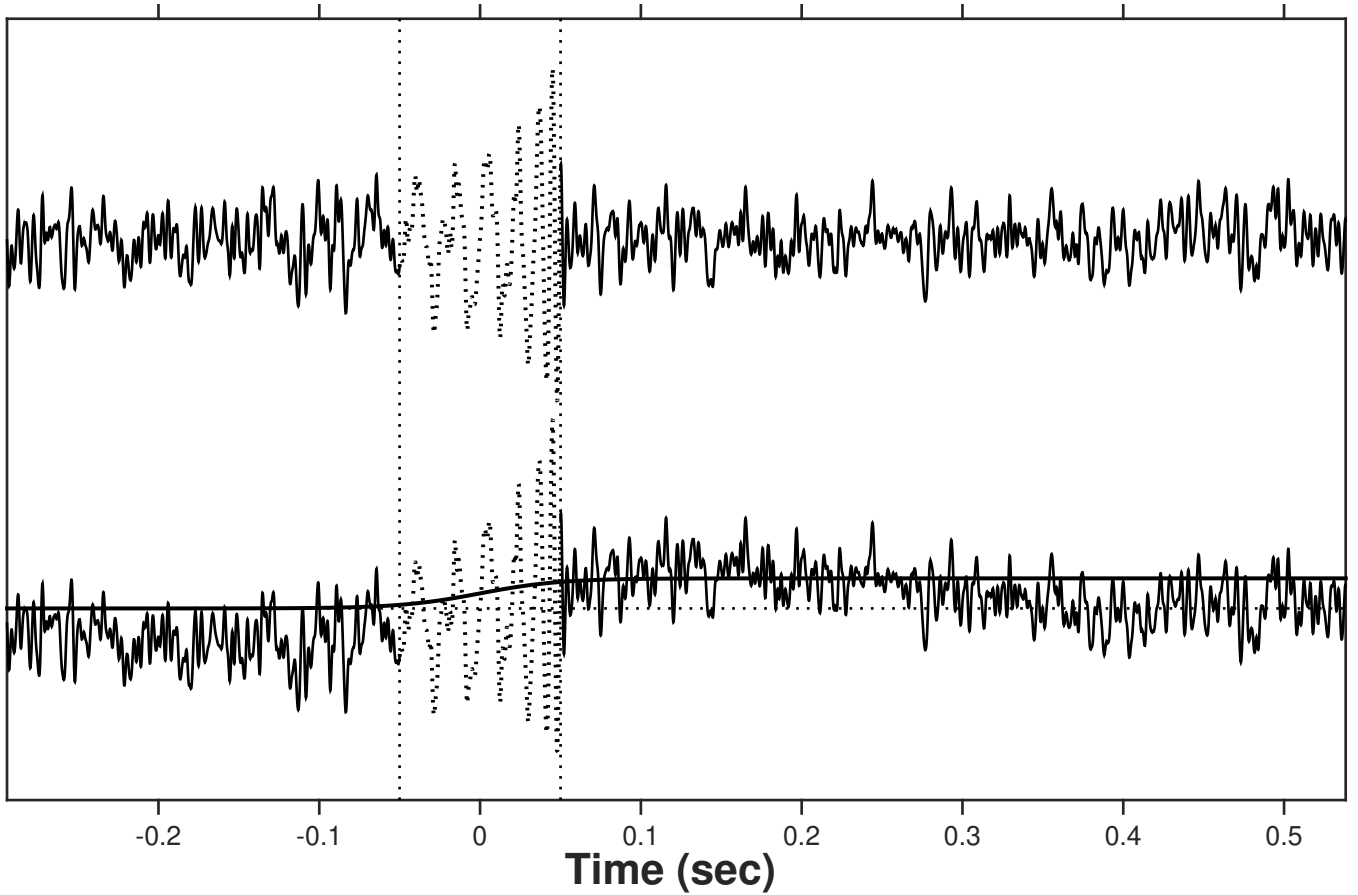


Figure 1. Hanford strain data for GW 150914, centered, whitened using a first-order Slepian taper, and low pass filtered at 200 Hz; amplitude scale arbitrary. Bottom: A *hyperbolic tangent* step function (smooth solid line) has been added to the same input data as in the top panel, and processed in the same way.

² Other than its use here in motivating averaging choices, this toy model is not used in the analysis.

3.2. Averaging Methods

The median was adopted as the metric for strains in the pre-event intervals due to its well-known *robustness* (Claerbout and Muir 1973), i.e. insensitivity to outliers. Four estimators were considered.

- (a) a weighted mean emphasizing the earlier times via the weight function $w(t) = (t - t_1)/(t_2 - t_1)$, where t_1 and t_2 denote the beginning and end of the post-event averaging interval;
- (b) the peak value (i.e. at $t = t_1$) of a linear fit to the strain as a function of time
- (c) the median value
- (d) the mean value

all evaluated over the same post-merger interval defined in §3.1. The first two aim to explicitly capture the reversion demonstrated in Fig. (1). Method (c) benefits from the robustness that influenced the choice for the pre-merger interval (where reversion is not present, so (a) and (b) are meaningless). All four are reported here, but the first two should be taken as more reliable (cf. the right-hand panel of Figure 3 of §5).

The resulting estimate of the *relative strain offset* is defined as the difference in strain averaged over the pre- and post- intervals, divided by the maximum absolute value of the strain during the event:

$$\text{Relative Strain Offset} \equiv \frac{h(\text{post-event}) - h(\text{pre-event})}{h_{\max}} = \frac{\Delta h_{\text{mem}}}{h_{\max}}. \quad (2)$$

This scaling not only provides a reliable self-calibration, but is the quantity most often discussed in the theoretical literature.

4. RESULTS

A number of specific pre-processing procedures have been detailed in §2: 4 tapers, 3 whitening schemes, and 9 high-frequency cutoffs, yielding a total of 108 combinations. These procedures were evaluated using the signal-to-noise in the cleaned data they each yielded when applied to the 64 time series. Specifically the metric for comparison was

$$\text{Signal-to-Noise} = \frac{\text{Recovered Event Amplitude}}{\text{Noise Standard Deviation}}, \quad (3)$$

the numerator being the absolute range of the event signal, and the denominator is evaluated over intervals bracketing, but excluding, the event itself. The resulting optimum cleaning methods and their parameters varied widely from observation to observation, and no single choice could be singled out as generally best. This circumstance is almost certainly due to the marked inhomogeneity, not readily apparent in strain plots, of the character of the noise. That is to say, not only does the seismic and other noise have unusual, non-Gaussian behavior, but its character varies from observation to observation. This motivates an adaptive approach, i.e. a procedure that automatically adjusts to the vagaries of the noise. To be specific, each of the observations described in §2.1 was pre-processed with the tapering, whitening and filtering method optimizing the signal-to-noise for that individual observation.

In each case statistical uncertainties were assessed in a way similar to that commonly used to estimate false detection rates for merger events. Data time-shifted in 0.5 second steps covering the 1024 seconds centered on the event (i.e. $\frac{1}{4}$ of the full 4096 seconds, but skipping one on either side of the event) were analyzed in exactly the same way as the non-shifted data. This is much like scanning a template – consisting of the “before” and “after” intervals separated by a gap corresponding to the merger event – along the data. The main difference from standard event search using templates is that the time of the event is known a priori; the important thing here is the response of the template to the noise presumed to surround it. In particular, random errors are quantified using the standard deviations of the resulting set of 2046 strain offset measures, and shown as 1σ standard errors in Table 1. These values do not include uncertainty in the maximum event strain in the denominator of Eq. (2), which has the role of a normalization factor. In addition false detection probabilities (FDPs) were determined from the fraction of offsets, determined from the time-shifted ensemble, larger than in the un-shifted data. Obviously this method loses accuracy for fractions $\sim 1/2046 = .0005$. The FDPs reported here have the important advantage of being independent of the error distribution, as opposed to standard errors which rely on Gaussianity.

Figure 2 and Table 1 summarize the strain offset estimates and their uncertainties. The four estimators for the post-event strain outlined in §3.1 are exhibited to highlight the moderate dependence on method, probably due mainly to differing responses to noise fluctuations. The weighted mean and linear fit are designed to be sensitive to the reversion noted in connection with Fig. (1). Hence these and the robust median are perhaps more reliable than the simple unweighted mean. The z-scores (i.e. ratios of the standard errors to the estimates), not listed in the table but plotted in Figure 2, range from < 1 , to be regarded as upper limits, to values above 2 and approaching 3, i.e. detections with the corresponding statistical significance.

Table 1. Statistics of Strain Offsets

No.	ID	Code	Strain Offsets (percents)					
			Weighted Average		Linear Fit		Median	
			$\Delta h \pm \sigma$	(FDP)	$\Delta h \pm \sigma$	(FDP)	$\Delta h \pm \sigma$	(FDP)
1	150914	HS2NOv-250	$+2.1 \pm 3.3$		$+1.1 \pm 5.0$		$+3.0 \pm 3.2$	0.33
2		LS2NOv-300	-0.8 ± 3.6		$+1.7 \pm 5.5$		-2.5 ± 3.5	
3	151012	HS1Ov-100	-5.6 ± 9.8		-13.4 ± 14.3		$+3.6 \pm 9.6$	
4		LS3P-100	-3.4 ± 10.7		-7.6 ± 15.3		$+1.3 \pm 10.5$	
5	151226	LTNOv-500	$+1.1 \pm 8.2$		-1.1 ± 11.9		$+3.1 \pm 8.0$	0.22
6	170104	HS2Ov-150	-11.6 ± 7.0		-21.3 ± 9.8		-1.8 ± 6.8	
7		LS2Ov-100	$+16.9 \pm 8.5$	0.13	$+24.0 \pm 12.0$	0.12	$+14.7 \pm 8.3$	0.17
8	170608	LS1NOv-500	$+0.8 \pm 7.7$		-3.2 ± 10.7		$+2.5 \pm 7.5$	0.47
9	170729	HTNOv-150	$+61.3 \pm 25.0$	0.04	$+65.8 \pm 36.4$	0.08	$+61.7 \pm 24.8$	0.04
10		LS2P-100	-12.7 ± 7.2		-18.8 ± 10.4		-0.0 ± 7.1	
11	170809	HTP-500	-41.6 ± 16.5		-31.1 ± 23.8		-41.3 ± 16.3	
12	170814	HS3P-500	-7.7 ± 11.0		-11.3 ± 15.9		-8.6 ± 10.9	
13		LTOv-100	$+7.9 \pm 8.3$	0.41	$+9.2 \pm 12.0$		$+6.4 \pm 8.2$	0.48
14		VS1NOv-300	$+30.8 \pm 11.6$	0.02	$+61.1 \pm 16.8$	0.00	$+20.8 \pm 11.5$	0.08
15	170818	LS1P-100	-1.7 ± 6.7		-4.5 ± 9.5		$+3.6 \pm 6.6$	
16	170823	HS1P-100	$+22.3 \pm 8.4$	0.16	$+27.8 \pm 12.0$	0.21	$+18.9 \pm 8.3$	0.19
17		LS1P-100	$+2.9 \pm 7.9$		$+0.4 \pm 11.3$		$+2.5 \pm 7.7$	
18	190408	HTP-100	-3.1 ± 8.7		-5.8 ± 12.4		-1.1 ± 8.5	
19		LS1P-350	$+1.6 \pm 6.1$	0.27	$+1.6 \pm 8.7$		$+1.8 \pm 6.0$	0.21
20	190412	LS2Ov-200	-3.5 ± 40.5		-4.4 ± 58.0		-3.6 ± 39.8	
21	190413	HS1NOv-350	-26.4 ± 54.6		-28.0 ± 78.3		-23.6 ± 53.6	
22		LS2P-300	$+4.0 \pm 4.9$		$+2.8 \pm 7.1$		$+4.5 \pm 4.8$	0.46
23	190421	LTP-200	$+1.0 \pm 6.3$		$+1.2 \pm 9.0$		$+3.6 \pm 6.1$	0.29
24	190424	LS2P-100	$+7.8 \pm 8.2$	0.05	$+17.5 \pm 12.0$	0.03	$+1.3 \pm 8.2$	
25	190503	HS2NOv-100	-14.7 ± 13.9		-12.7 ± 20.3		-17.1 ± 13.8	
26		LTNOv-100	$+31.3 \pm 19.0$		$+57.0 \pm 27.0$	0.29	$+24.0 \pm 19.0$	
27	190512	HS3P-500	-2.0 ± 14.4		-3.4 ± 20.4		-1.7 ± 14.3	
28		LS1NOv-200	$+0.1 \pm 35.4$		-0.9 ± 50.4		$+0.4 \pm 35.2$	
29	190514	HS2Ov-100	$+7.9 \pm 28.6$	0.36	$+9.8 \pm 40.7$		$+11.4 \pm 28.4$	0.15
30	190517	LS1Ov-100	$+20.1 \pm 7.9$	0.08	$+21.5 \pm 11.4$	0.17	$+19.3 \pm 8.0$	0.09
31	190519	HS2NOv-100	$+6.6 \pm 15.3$	0.42	$+3.9 \pm 22.1$		$+7.1 \pm 15.5$	0.34
32	190521	LTP-100	-1.8 ± 14.9		-5.3 ± 21.6		-0.9 ± 15.1	
33		HS2NOv-100	-1.5 ± 12.7		$+3.0 \pm 18.5$		-8.3 ± 12.9	
34		LS1Ov-100	$+1.1 \pm 6.4$		-2.8 ± 9.4		$+1.7 \pm 6.5$	
35	190527	HTP-500	-1.4 ± 7.6		$+0.2 \pm 11.1$		-5.2 ± 7.7	
36		LS1NOv-100	-8.7 ± 9.4		-10.7 ± 13.7		$+2.1 \pm 9.5$	
37	190602	HS1P-100	-11.5 ± 8.4		-19.1 ± 12.3		-5.9 ± 8.5	
38		LS1NOv-500	$+0.3 \pm 11.9$		-0.6 ± 17.4		-1.7 ± 11.9	
39	190620	LS1NOv-100	$+5.1 \pm 14.6$	0.18	$+0.6 \pm 21.4$		$+6.9 \pm 14.6$	0.06
40	190630	LS2Ov-100	$+3.3 \pm 16.9$	0.10	$+9.0 \pm 24.8$	0.02	-0.9 ± 17.0	
41	190701	HS2NOv-500	$+4.1 \pm 9.2$	0.36	$+5.4 \pm 13.5$	0.49	$+1.6 \pm 9.2$	
42		VTP-500	$+9.1 \pm 9.1$	0.12	$+5.8 \pm 13.4$		$+9.3 \pm 9.1$	0.09
43	190706	HS2NOv-400	-1.4 ± 9.4		-8.8 ± 13.8		$+3.3 \pm 9.4$	
44		LS1NOv-100	-11.0 ± 12.7		-6.3 ± 18.8		-12.3 ± 12.5	
45	190707	HS1NOv-500	-1.2 ± 22.8		-2.8 ± 33.7		$+0.5 \pm 22.5$	

Continuation of Table 1

			Strain Offsets (percents)							
No.	ID	Code	Weighted Average		Linear Fit		Median		Mean	
46		LS2NOv-500	-0.7 ± 14.4		-0.2 ± 21.4		-0.2 ± 14.3		-0.2 ± 13.3	
47	190708	LS3Ov-100	-5.8 ± 33.0		-9.5 ± 48.9		-5.3 ± 32.6		-5.3 ± 30.5	
48	190727	HS2NOv-250	$+8.1 \pm 16.1$	0.11	$+20.7 \pm 23.9$	0.01	$+4.5 \pm 16.1$	0.32	$+4.5 \pm 14.9$	
49		LTP-100	$+21.1 \pm 16.6$	0.00	$+35.1 \pm 24.6$	0.00	$+15.8 \pm 16.6$	0.02	$+15.8 \pm 15.3$	0.03
50	190728	HS3P-400	-3.3 ± 14.8		-7.0 ± 22.0		-3.5 ± 14.8		-3.5 ± 13.7	
51		LTP-300	$+0.7 \pm 15.2$	0.49	$+2.5 \pm 22.5$	0.13	-0.5 ± 15.1		-0.5 ± 14.0	
52	190803	HS2NOv-100	-2.7 ± 39.4		-0.1 ± 58.9		-5.0 ± 38.8		-5.0 ± 36.0	
53	190828	HS2Ov-100	-1.1 ± 5.2		-1.1 ± 7.8		-0.4 ± 5.1		-0.4 ± 4.8	
54		LS1Ov-100	$+3.3 \pm 8.1$	0.17	$+5.0 \pm 12.1$	0.23	$+3.4 \pm 8.0$	0.14	$+3.4 \pm 7.4$	0.22
55	190909	HS1Ov-100	$+1.8 \pm 17.3$		$+9.3 \pm 26.0$		-3.9 ± 17.1		-3.9 ± 15.8	
56		LS1Ov-500	$+19.9 \pm 23.4$	0.12	$+27.0 \pm 35.0$	0.13	$+16.8 \pm 23.0$	0.18	$+16.8 \pm 21.4$	0.17
57	190910	LS1NOv-100	$+3.3 \pm 4.1$	0.13	-0.0 ± 6.1		$+5.0 \pm 4.0$	0.03	$+5.0 \pm 3.7$	0.01
58	190915	HS3NOv-100	-0.4 ± 11.4		$+7.5 \pm 17.1$		-9.1 ± 11.2		-9.1 ± 10.4	
59		LTP-100	-1.2 ± 11.3		-3.1 ± 16.9		-1.0 ± 11.1		-1.0 ± 10.3	
60	190929	HTOv-100	$+4.0 \pm 7.9$	0.47	$+7.5 \pm 11.9$	0.47	$+0.9 \pm 7.8$		$+0.9 \pm 7.2$	
61		LTP-100	-0.8 ± 7.8		-1.3 ± 11.9		-1.9 ± 7.7		-1.9 ± 7.1	
62	191223	LS1NOv-100	-2.7 ± 6.7		-6.7 ± 10.2		-0.8 ± 6.6		-0.8 ± 6.1	
63	191225	VTP-100	-2.8 ± 6.6		-8.7 ± 10.0		-0.5 ± 6.4		-0.5 ± 6.0	
64	200114	LS1NOv-100	$+0.3 \pm 3.3$		-0.1 ± 5.0		$+0.7 \pm 3.2$	0.43	$+0.7 \pm 3.0$	

Note: For each of the four strain offset metrics (weighted mean, linear fit, median and mean) the relative strain offset and its standard error (both percentages) are given, followed by the false detection probability (FDP) only if it is less than 0.5. In the code, OTW-F, O is the observatory (Hanford, Livingston, Virgo), and the optimization values are: T denotes the taper: T = Tukey, Sn = Slepian of order n; W indicates the whitening method: Ov = Welch, 2-second overlap, NO = Welch, no overlap, P = unsmoothed spectrum (“phase only”); and F is the low-pass cutoff frequency in Hz.

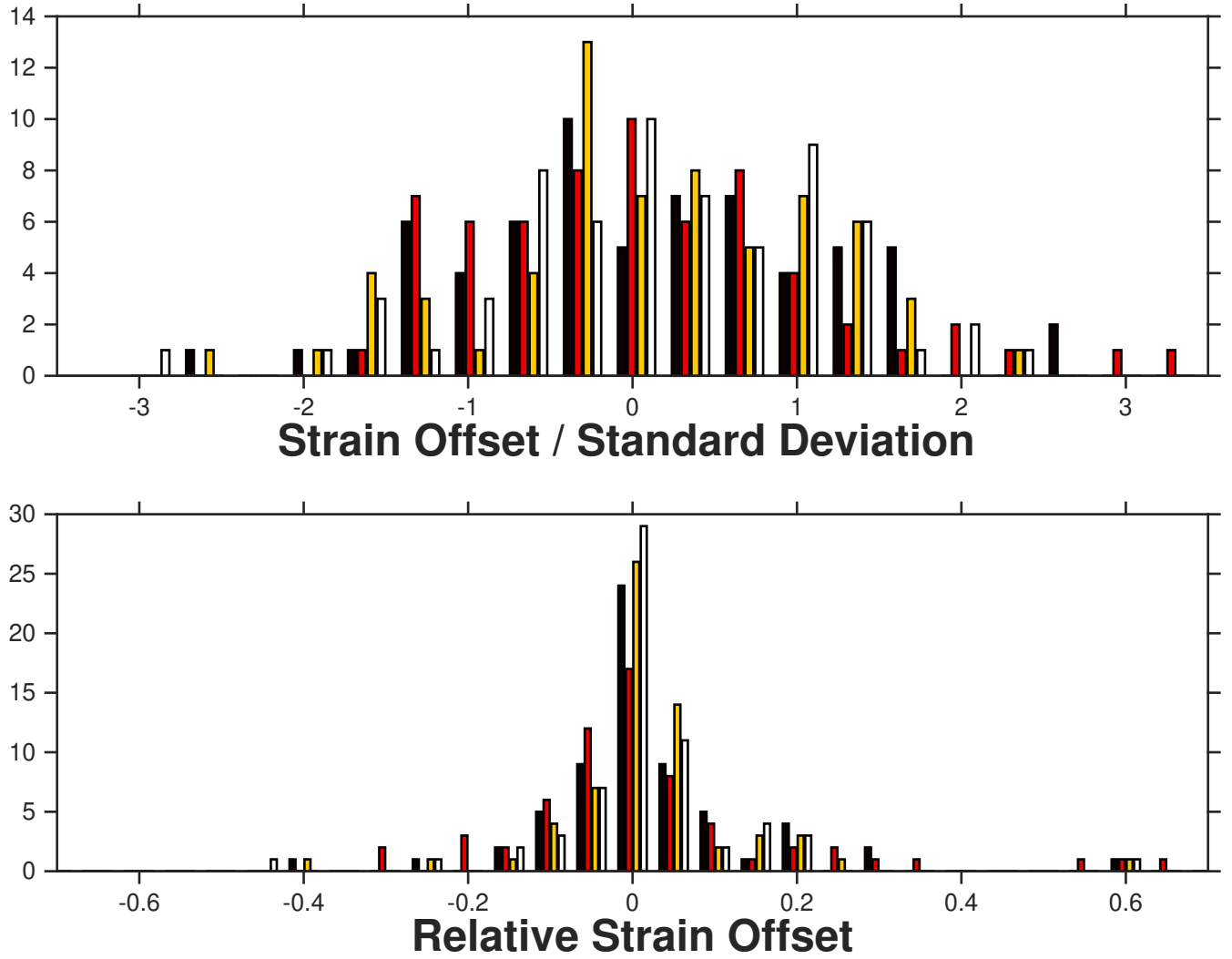


Figure 2. Distribution of the signed strain offset estimates from the 4 metrics: black = weighted mean; red = linear fit; yellow = median; white = mean. Top: *normal scores* (also known as *z-scores* or *pull* in high energy physics): the estimated offset Δh divided by the standard deviation from the time-shift analysis. Bottom: Relative strain offset: Δh_{mem} divided by the range of strains during the merger event.

5. CONCLUSIONS AND DISCUSSION

In several cases the analysis in §§2-4 yields probable detection of a permanent strain offset. The significance based on assessing random errors with the time-shift procedure is straightforward and should be reliable. But this is not the whole story. As always unknown systematic errors need to be considered. A large variability in the individually adopted pre-processing procedures (taper choice, whitening procedure, and low-pass cutoff frequency) was exhibited during the optimization study in §4, as depicted in the “code” in Table 1. This dependence – on known analysis parameters – is generated by heterogeneous strain errors, and is not a signature of unknown systematic error. In fact, to the extent that the sub-optimality of any pre-processing scheme (as judged e.g. relative to an ideal scheme, defined as the one most closely reproducing the true gravitational-wave signals) decreases the magnitude of the estimated memory offset, the offset estimates among the 108 cleaning schemes are lower limits.

In looking for potential analysis problems, it would seem that errors in setting the locations and lengths of the averaging intervals are the most likely potential sources of systematic error. Perhaps most serious would be mis-specification of the stop time of the merger event, for then spill-over of the merger signal could masquerade as a memory effect. The procedure described in §2.1 was designed to minimize this possibility.

Several additional results provide further support for a claim of detection of strain offsets. Both Hanford and Livingston observations passed the selection criteria in §2.1 for 21 of the events. For these cases the two strain offsets should be related, modulo orientation effects. The left-hand panel of Figure 3 shows the corresponding relation in the data taken from Table 1. The “sign-flip” (Abbott et al. 2016, the caption of Fig. 1) between Hanford and Livingston is accounted for here, but other orientation effects and the rather large observational errors and scatter preclude a definitive conclusion. However this plot is consistent with a correlation between the Hanford values and the negative of the Livingston values.

The estimates and standard deviations presented in Table 1 describe the statistical uncertainty of the individual strain offset estimates. But it is instructive to quantify in addition the statistics of the entire set of measurements. Such an analysis accounts for the *trials factor*³ or “look elsewhere” issue. In this context, the right-hand panel of Figure 3 quantifies the plausibility that measured memory offsets in the whole data set are significant and not simply values in the tails of the overall error distribution. A straightforward approach is to define some criterion of “success” for an ensemble of 64 measurements, and judge statistical uncertainty based on the success frequency in time-shifted measurements. A natural criterion is the number of offset measurements that exceed (in absolute value) a pre-defined threshold, as plotted in the right-hand panel of Figure 3. The mean and variance from the time-shifted data showed little dependence on cleaning method, and is shown as a solid band and surrounding dashed and dotted lines. The thick solid lines represent the actual data, with the four different metrics (a)-(d) in §5. The fact that these lines lie well above the error band indicates the significance of the detections at more than 3σ . Note that the preference for the first two metrics, argued for in §3.2 because they directly target the reversion feature of memory, is clearly evident here – in their superiority over the median and mean.

There is one more confirmatory piece of evidence. Depending on its slope, the linear fit described in §3.2 can represent either (a) the reversion to the pre-event strain level (characterizing a memory effect) or (b) growth away from it. Random noise would yield these properties in equal numbers. In fact rather strong statistical evidence for the presence of memory effects is provided by the preponderance of (a) – 53 cases, with only 11 cases of (b). Figure 4 depicts the cleaned strain around all of the observations with property (a) and FDP less than 0.2. In some cases, particularly in the first panel, the cleaning was clearly relatively poor, and the noise level is an important issue. Note that these samples were chosen based on their FDP, not the size of the estimated strain offset. The fact that in all eight of these cases the memory effect is positive is probably accidental; the distribution of for the full data set is more or less symmetric about zero (cf. the bottom panel in Figure 2).

The detections presented here could be validated in a rather definitive way if the relative strain offsets were to show a clear dependence on the energy radiated during the merger (cf. Braginsky and Thorne 1987; Favata 2009; Garfinkle 2016). With complications due to orientation effects, the limitations of the current data and uncertainties in the total mass, radiated mass, and orientation, this is not yet feasible.

Detection of even the simplified signature of GW memory embodied in the relative strain offset is difficult, limited largely by signal-to-noise. Improvements could include more sophisticated data cleaning techniques and a hybrid approach where the oscillatory merger signal is modeled and the memory sought in the residuals. And of course full modeling of all components, transitory and permanent, will ultimately achieve definitive tests for the relevant predictions of general relativity.

³ The statistics of results from an ensemble is affected in a way that depends on the effective number of independent trials.

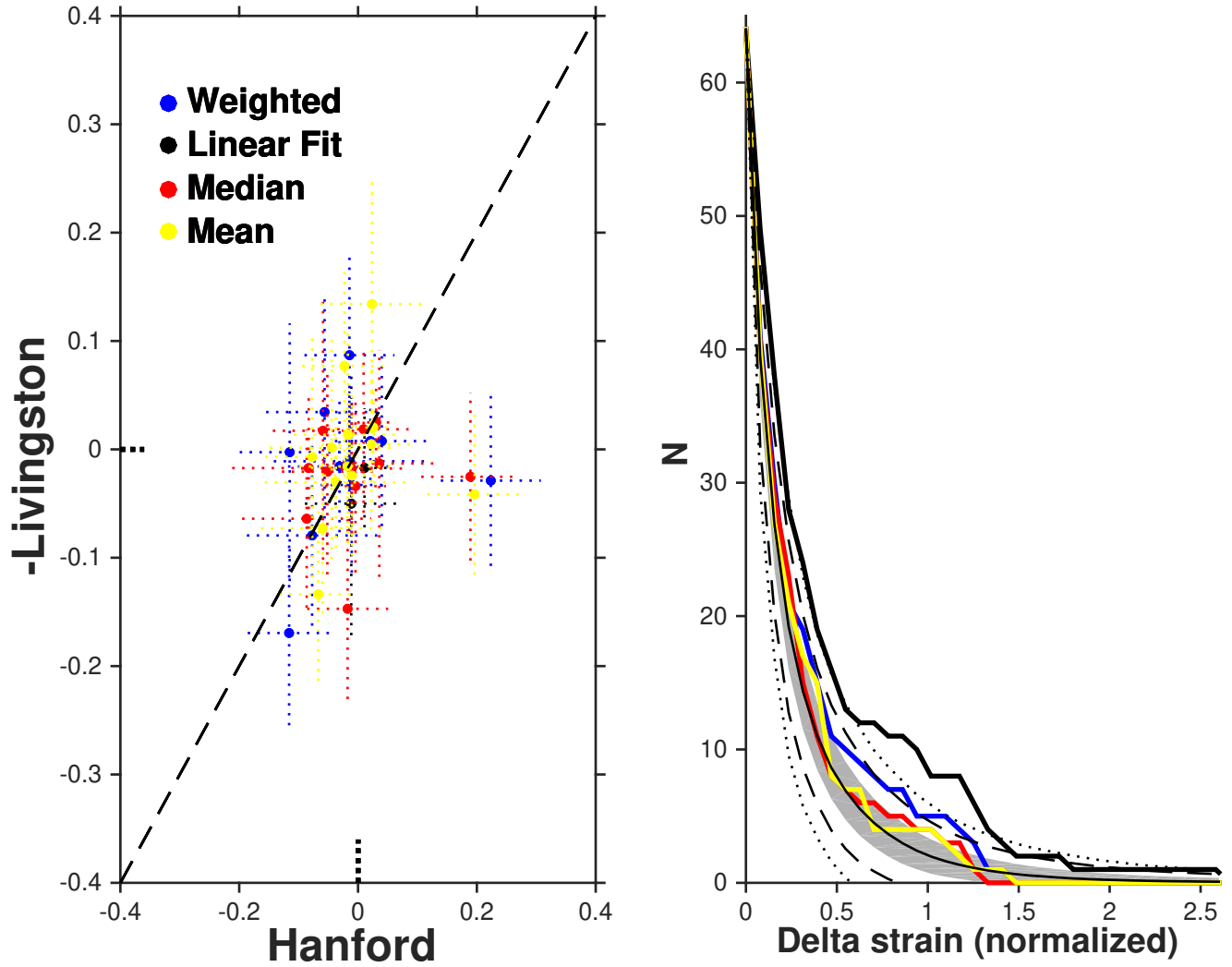


Figure 3. Left: Scatter plot of the relative strain offsets for 21 events with both Hanford and Livingston data. The negatives of the Livingston values are plotted against the Hanford ones, to account for the expected sign flip. Right: Number of ensemble successes (measurements exceeding threshold) as a function of a threshold that is normalized by the standard deviation of the cleaned strain. The solid band and surrounding dashed and dotted lines bracket $\pm 1\sigma$, $\pm 2\sigma$ and $\pm 3\sigma$ uncertainties in the time-shifted measurements. The solid lines are for the actual measurements with the 4 cleaning schemes, with the same color identification as in the left-hand panel.

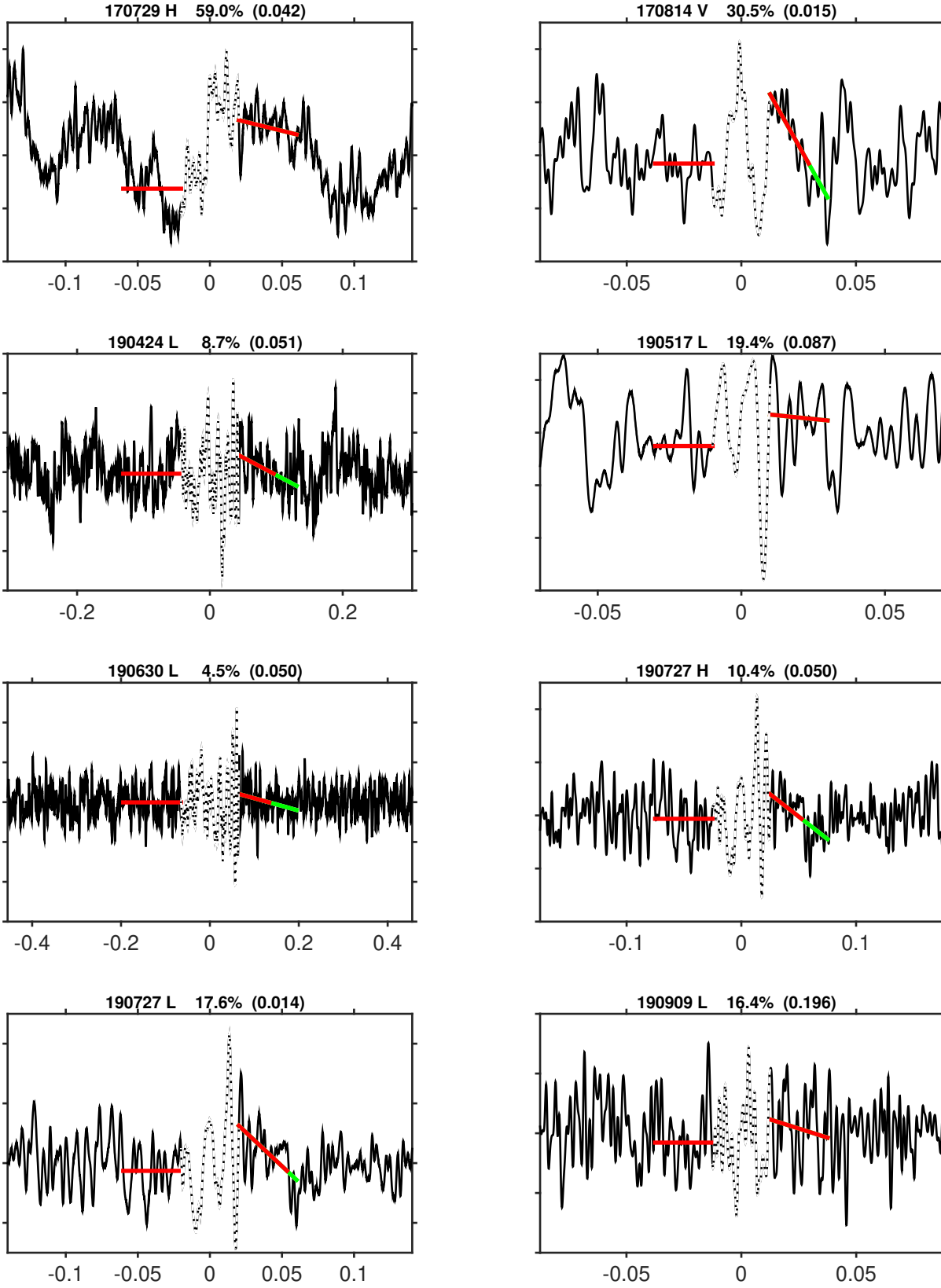


Figure 4. Cleaned time series with the strain in the event intervals as dotted lines. The median pre-event strain is plotted as a thick (red) line; the linear fit to the post-event strain is a similar line, switching color to green if and when it crosses the pre-event level. These are all of the observations with false detection probabilities less than 0.2 and linear fit slopes indicative of reversion to zero.

I am especially grateful to Bob Wagoner, Ben Farr and Keefe Mitman for important suggestions. Ron Adler, Sasha Buchman, Mike Ely, Gary Godfrey, Javier Pascual Granado, Ron Walton, Alex Silbergleit, Suwen Wang, and Paul Worden also provided helpful comments. Alan Weinstein, Ben Farr, Brian Lantz and other members of the GWOSC also provided useful data help. Many thanks to Joe Bredekamp, the NASA Applied Information Systems Research Program and the NASA Astrophysics Data Analysis Program (Grant NNX16AL02G) for support.

This research has made use of data obtained from the Gravitational Wave Open Science Center (<https://www.gwopenscience.org/>), a service of LIGO Laboratory, the LIGO Scientific Collaboration and the Virgo Collaboration. LIGO Laboratory and Advanced LIGO are funded by the United States National Science Foundation (NSF) as well as the Science and Technology Facilities Council (STFC) of the United Kingdom, the Max-Planck-Society (MPS), and the State of Niedersachsen/Germany for support of the construction of Advanced LIGO and construction and operation of the GEO600 detector. Additional support for Advanced LIGO was provided by the Australian Research Council. Virgo is funded, through the European Gravitational Observatory (EGO), by the French Centre National de Recherche Scientifique (CNRS), the Italian Istituto Nazionale di Fisica Nucleare (INFN) and the Dutch Nikhef, with contributions by institutions from Belgium, Germany, Greece, Hungary, Ireland, Japan, Monaco, Poland, Portugal, Spain.

REFERENCES

- Abbott, R. et al. (LIGO Scientific Collaboration and Virgo Collaboration), 2016, Observation of Gravitational Waves from a Binary Black Hole Merger Phys. Rev. Lett. 116, 061102
- Abbott, R. et al. (LIGO Scientific Collaboration and Virgo Collaboration), "Open data from the first and second observing runs of Advanced LIGO and Advanced Virgo", SoftwareX 13 (2021) 100658.
<https://www.gw-openscience.org/eventapi/html/allevnts/>
- Acton, F. 1990, Numerical Methods that [usually⁴] Work; Interlude: What Not to Compute, p. 253, Mathematical Association of America: Washington
- Bian, L., Cai, R., Cao, S., Cao, Z., Gao, H., Guo, Z., Lee, K., Li, D., Liu, J., Lu, Y., Pi, S., Wang, J., Wang, S., Wang, Y., Yang, T., Yang, X., Yu, S., and Zhang, X., The Gravitational-Wave Physics II: Progress, arXiv:2106.10235
- Boersma, O., Nichols, D. and Schmidt, P. 2020, Forecasts for detecting the gravitational-wave memory effect with Advanced LIGO and Virgo, Phys. Rev. D 101, 083026 (2020), arXiv:2002.01821
- Braginsky, V., Thorne, K. Gravitational-wave bursts with memory and experimental prospects. Nature 327, 123–125 (1987). <https://doi.org/10.1038/327123a0>
- Claerbout, J. and Muir, F. 1973, Robust Modeling with Erratic Data, Geophysics, 38, 812-985
- Divakarla, A. and Whiting, B. 2021, The First-Order Velocity Memory Effect from Compact Binary Coalescing Sources, arXiv:2106.05163
- Favata, M. 2009, J. Phys. Conf. Ser. 154, 012043
- Favata, M. 2010, Class. Quant. Grav. 27:084036; see also <http://www.phy.olemiss.edu/StrongBaD/talks/Favata.pdf>
- Flanagan, E., Grant, A., Harte, A. and Nichols, D. 2019, Persistent gravitational wave observables: General framework Phys. Rev. D, 99, 084044
- Flanagan, E., Grant, A., Harte, A. and Nichols, D. 2020, Persistent gravitational wave observables: Nonlinear plane wave spacetimes Phys. Rev. D, 101, 104033
- Garfinkle, D. 2016, A simple estimate of gravitational wave memory in binary black hole systems, arXiv:1605.06687
- Grant, A. and Nichols, D. 2021, Persistent gravitational wave observables: Curve deviation in asymptotically flat spacetimes, arXiv: 2109.03832
- Hübner, M., Talbot, C., Lasky, P. and Thrane, E. 2020, Measuring gravitational-wave memory in the first LIGO/Virgo gravitational-wave transient catalog Phys. Rev. D 101, 023011
- Hübner, M., Paul Lasky, and Eric Thrane, E. 2021, Memory remains undetected: Updates from the second LIGO/Virgo gravitational-wave transient catalog Phys. Rev. D 104, 023004
- Islo, K., Simon, J., Burke-Spolaor, S., and Siemens, X. 2019, Prospects for Memory Detection with Low-Frequency Gravitational Wave Detectors, arXiv:1906.11936
- Johnson, A., Kapadia, S., Osborne, A., Hixon, A., and Kennefick, D. 2019, Prospects of detecting the nonlinear gravitational wave memory," Phys. Rev. D 99, 044045 (2019), arXiv:1810.09563 [gr-qc].
- Kennefick, D. 1994, Prospects for detecting the Christodoulou memory of gravitational waves from a coalescing compact binary and using it to measure neutron star radii, Phys. Rev. D 50, 3587–3595 (1994).
- Khera, N., Krishnan, B., Ashtekar, A. and De Lorenzo, T. (2021) Inferring the gravitational wave memory for binary coalescence events Physical Review D, 103, 044012
- Lasky, P., Thrane, E., Levin, Y., Blackman, J/, and Chen, Y. 2016, Detecting gravitational wave memory with LIGO: implications of GW150914, Phys. Rev. Lett. 117, 061102 (2016), arXiv:1605.01415
- Liu, X., He, X., and Cao Z., 2021, Accurate calculation of gravitational wave memory, Phys. Rev. D 103, 043005
- McKechan, D., Robinson, C. and Sathyaprakash, B. 2010, A tapering window for time-domain templates and simulated signals in the detection of gravitational waves from coalescing compact binaries Class.Quant., 27:084020
- Mitman, K., Iozzo, D., Khera, N., Boyle, M., De Lorenzo, T., Deppe, N., Kidder, L., Moxon, J., Pfeiffer, H., Scheel, M., Teukolsky, S., and Throwe, W. 2021, Adding gravitational memory to waveform catalogs using BMS balance laws, Physical Review D, Volume 103, Issue 2, article id.024031
- Percival, D., and Walden, A. 1993, Spectral Analysis for Physical Applications: Multitaper and Conventional Univariate Techniques. Cambridge: Cambridge University Press, 1993.
- Pollney, D. and Reisswig, C.(2011), Gravitational Memory in Binary Black Hole Mergers, ASP. J., 732, L13,

⁴ Amusingly this word is lightly embossed on the cover of some editions.

- Slepian, D, 1978, Prolate spheroidal wave functions, fourier analysis, and uncertainty — V: the discrete case,” The Bell System Technical Journal, 57, 1371-1430
- Spectrum estimation and harmonic analysis, Thomson, D. J. (1982) Proceedings of the IEEE, 70, 1055–1096
- Thorne, K. Gravitational-wave bursts with memory: The Christodoulou effect, 1987, Physical Review D, 45, 520
- Yang, H. and Martynov, D(2018) Testing Gravitational Memory Generation with Compact Binary Mergers, Physical Review Letters, 121, 071102
- Zhang, P., Duval, C., Gibons, G. and Horvathy, P., 2017, Physics Letters B, 772, 743
- Zhao, Z., Liu, X., Cao, Z. and He, X., 2021) Gravitational wave memory of the binary black hole events in GWTC-2, Physical Review D., 104, 064056